AIAA JOURNAL
Vol. 45, No. 5, May 2007

Development of a Computational Hydrodynamic Model for a Biomimetic Underwater Autonomous Vehicle

Samuel F. Galls* and Othon K. Rediniotis†
Texas A&M University, College Station, Texas 77843-3141

DOI: 10.2514/1.10060

This work describes the development of a computational model created to autonomously navigate a fishlike underwater vehicle with a multivertebra spine and a flexible tail. First, a two-dimensional numerical simulation, developed previously, and based on an unsteady panel method, was coupled with the vehicle, spine, and tail dynamics. Numerous test cases spanning a wide range of swimming conditions were processed with the simulation, and these data were subsequently used to train an artificial neural network. The navigation procedure/neural network uses as input a set of vehicle geometric and state variables, and from that, it predicts the needed vehicle body deformations, i.e., necessary spine vertebrae rotations, so that the vehicle can navigate through a set of given waypoints. Validation results are presented that show the accuracy of the present flow-structure interaction solver, and several test cases of autonomous navigation are presented to show the capabilities of the current method.

Nomenclature

$\boldsymbol{A}$	=	reaction force vector at each joint
$\hat{\boldsymbol{a}}$	=	six element vector containing $\boldsymbol{a}$ and $\boldsymbol{\alpha}$
$\boldsymbol{a}$	=	linear acceleration vector of each link
ax, ay, az	=	components of vector $\boldsymbol{a}$
$B1, B2$	=	transformation matrices from previous vehicle link
$\hat{\boldsymbol{C}}$	=	six element vector containing the Coriolis terms for each link
c	=	chord or body length
D	=	torsional damper constant for each joint in the free tail
$\hat{\boldsymbol{d}}$	=	six element vector containing the distance from a link's joint to its center of mass
dx, dy, dz	=	variable components of $\hat{\boldsymbol{d}}$
$\boldsymbol{F}$	=	force vector acting on vehicle
Fx, Fy, Fz	=	components of vector $\boldsymbol{F}$
$\boldsymbol{F}'$	=	fluid force vector acting on each link
$\hat{\boldsymbol{F}}$	=	six element vector containing the external loads $\boldsymbol{F}'$ and $\boldsymbol{T}$
$\boldsymbol{f}$	=	total force vector acting on the center of mass of each joint
$\hat{\boldsymbol{f}}$	=	six element vector containing $\boldsymbol{f}$ and τ
fx, fy, fz	=	components of vector $\boldsymbol{f}$
g	=	acceleration of gravity
h_p	=	distance during plunge
I	=	inertia of vehicle
I'	=	rotational inertia of each link
I_x, I_y, I_z	=	diagonal components of the inertia matrix for each link
I_{xy}, I_{xz}, I_{yz}	=	off-diagonal components of the inertia matrix for each link
i	=	time index during navigation, body index
j	=	waypoint index
K	=	trailing edge nondimensional angular deflection rate
Kt	=	torsional spring constant for each joint in the free tail
k	=	time index in flow/dynamics solver
L	=	length of each link
$\boldsymbol{L}$	=	length vector of each link in the inertial frame
$\boldsymbol{M}$	=	moment acting on vehicle with respect to the center of mass
$\boldsymbol{M_A}$	=	reaction moment acting at each joint
$\boldsymbol{M_D}$	=	moment from the torsional damper acting at each joint
$\boldsymbol{M}_{\mathbf{joint}}$	=	total moment vector acting at each joint
$\boldsymbol{M_K}$	=	moment from the torsional spring acting at each joint
m	=	mass of vehicle
$\boldsymbol{m}$	=	mass-inertia matrix for each link
m'	=	mass of individual links
N	=	total number of vehicle links (includes body and tail links)
n	=	number of main/actuated body links
Q	=	magnitude of torque required at each joint per unit span
q	=	joint angle
$\boldsymbol{R}$	=	position vector of the vehicle in the inertial frame
$\boldsymbol{r}_{cg}$	=	position vector of the center of mass of each link in the inertial frame
$\boldsymbol{r}$	=	vector between centers of mass of two adjacent links in the vehicle
rx, ry, rz	=	components of vector $\boldsymbol{r}$
s	=	distance along vehicle camber/centerline
$\hat{\boldsymbol{s}}$	=	transformation matrix
s_1, s_2	=	limits in the camber where the angle variation occurs in the vehicle
$\boldsymbol{T}$	=	external moment vector acting on the center of mass of each link
T_x, T_y, T_z	=	components of vector $\boldsymbol{T}$
t	=	time
V	=	vehicle velocity magnitude
$\boldsymbol{V_o}$	=	vehicle velocity vector in the inertial frame
$\boldsymbol{V}'$	=	velocity vector of individual link center of mass
wx, wy	=	waypoint coordinates in the inertial frame
Xcg, Ycg	=	coordinates of center of mass of complete vehicle
x, y	=	position in the inertial frame
xcg, ycg	=	coordinates of center of mass of each link

Received 28 March 2005; revision received 24 August 2006; accepted for publication 24 December 2006.

*Research Associate, Aerospace Engineering Department. Associate Member AIAA.
†Associate Professor, Aerospace Engineering Department. Associate Fellow AIAA.

$\boldsymbol{\alpha}$	=	angular acceleration vector of each link
$\alpha x, \alpha y, \alpha z$	=	components of vector $\boldsymbol{\alpha}$
ΔT	=	sampling time during navigation procedure
$\Delta T_3, \Delta T_4$	=	time steps used in tail deflection history for navigation training
ΔTa	=	time duration for acceleration maneuver
Δt	=	time step
$\underline{\Delta x}, \underline{\Delta y}$	=	relative horizontal and vertical positions
$\overline{\Delta x}, \overline{\Delta y}$	=	normalized relative horizontal and vertical positions
$\Delta\theta$	=	change in body pitch
δ_1, δ_2	=	link angles for dynamics validation case
θ	=	body pitch or rotation angle with respect to the inertial frame
θ_{LE}	=	leading edge deflection with respect to the body centerline
$\theta_{\max}$	=	maximum tail root deflection during an acceleration maneuver
θ_{TE}	=	trailing edge deflection with respect to the body centerline
θ_{TEroot}	=	tail root deflection with respect to the body centerline
τ	=	total moment acting on the center of mass of each link
$\tau x, \tau y, \tau z$	=	components of the moment acting on each vehicle joint
$\boldsymbol{\Omega}$	=	angular velocity vector of vehicle
$\boldsymbol{\omega}$	=	angular velocity vector of each link
$\boldsymbol{\omega} x, \boldsymbol{\omega} y, \boldsymbol{\omega} z$	=	angular velocity vector components of each vehicle link

Introduction

IN RECENT years, considerable interest has focused on the development of highly maneuverable underwater vehicles with their design being based on the swimming techniques (undulatory and labriform locomotion) and anatomic structure of fish [1]. Reviews of studies on fin appendages, the dynamics of slender fish, the propulsion mechanisms of fish motion, slender wings and thin plates with passive and active chordwise flexibility, and similar topics can be found in [1–3]. A brief review of some of the relevant efforts is also given here.

Lighthill [4] applied the slender body theory of hydrodynamics to transverse oscillatory motions of slender fish, resulting in the elongated body theory. Jones and Platzer [5] investigated plunging and pitching airfoils and showed that plunging always produced thrust and pitching produces thrust only at low frequencies. Another two-dimensional study concerning the motion of a fish tail was the work performed by DeLaurier and Harris [6]. They plunged and pitched an airfoil and recorded the thrust generated. They showed that the plunging thrust could also be explained by the leading edge (LE) suction force. In addition, if pitching and plunging are performed at the same time, thrust can be generated by the streamwise component of the airfoil's normal force leading to larger thrust. The largest thrust from the airfoil was achieved when the pitch angle was negative at its maximum plunge deflection. A flexible plate that simulated the spine of a trout was tested in a water tunnel by Kelly [7]. He demonstrated that for a sinusoidal waving plate the thrust starts when the running wave speed was about the same as the flow speed. If the plate oscillated slowly there was drag (not accounting for skin friction drag). Thrust was present if the plate oscillated with a wave speed greater than or equal to the flow speed. Kelly also showed that the efficiency decreased as the wave velocity increased above the flow velocity because of power dissipation into the wake.

Besides cruise swimming, other maneuvers that are of interest for the current application are turning and acceleration through fast starts. Weihs [8] noted that a fish turn is composed of three main stages. A turn starts with the head rotating causing momentum changes, then the body flexes while the tail stays aligned with the flow, and finally the body straightens the tail, pushing the fish in the desired direction. In the case of fast starts, which are common in predator–prey situations, Beddow et al. [9] note that a fast start also has three stages. Stage 1 is a preparatory stroke, during which the tail is moved laterally with respect to the body axis and forms an S or C-shaped start position. Stage 2 occurs when the tail is moved through one complete beat cycle, during which most of the thrust is generated; this is considered the propulsive stage. Stage 3 is a glide of variable duration and sometimes is the prelude to a steady swimming sequence. Although these maneuvers are easily performed by fish, it can be difficult to exactly reproduce the same motion in an underwater vehicle. Certain simplifications, however, can be imposed to the structure and control of a synthetic vehicle to sufficiently accurately replicate, understand, and model related biomimetic principles.

Navigation control of such fishlike vehicle involves a large number of variables and the relationships between actuation of the several mechanical parts and the fluid forces on the vehicle are typically nonlinear and complicated to formulate. Artificial neural networks (ANN) can be used to deal with this complexity. Artificial neural networks simulate their biological counterparts. They simulate human and animal cognition and decision-making mechanisms and the processes for learning [2,3]. Since the discovery of a powerful training algorithm, the back-propagation algorithm [10] in 1986, artificial neural networks have received increasing attention by scientific communities, including aerodynamicists and fluid mechanicians. ANN have been shown to successfully model a wide diversity of aero/hydrodynamics processes and systems. They have successfully: encoded three-dimensional unsteady separated flowfield dynamics [11,12], used with flight air-data systems [13], controlled transition to turbulence [14], formulated calibration algorithms for flow diagnostics instrumentation [15,16], and achieved order reduction and navigation in vehicle hydrodynamics problems [2,3].

The objective of the present work is to develop a numerical model of the hydrodynamics and structural dynamics aspects, as well as their interactions, of mechanical, fishlike underwater vehicles, that emulate the anatomic structure and undulatory swimming techniques of fish. Such anatomic features include a multivertebra spine and a flexible tail. The work then uses this model to formulate, through the use of artificial neural networks, navigation algorithms for the vehicle. Compared with the work presented in [2], there are several innovations implemented in the present effort. First, unlike the vehicle tail in [2], the tail of the present vehicle simulates that of a fish more accurately; it is flexible and is allowed to respond to the main body/spine motions and the resultant hydrodynamic forces. Also, the present simulation yields the necessary actuation torques (actuators are simulated at every spine joint, i.e., at the point where two adjacent vertebrae join each other) to achieve the necessary body/spine deformation. This was motivated by our need to properly control the shape-memory-alloy actuators that were controlling the spine motion in the vehicle of [17].

Vehicle Geometry and Kinematics

In the development of the vehicle geometry, there are two main goals that need to be met. The first goal is to have a proper approximation of a reference mechanical model with respect to its structure, and the second goal is to have kinematics that could properly simulate typical maneuvers of turning, swimming, and fast starts of fish.

Structure

The geometry of the vehicle is referenced, only approximately, to the mechanical model of [17], also shown in Fig. 1. This model is made of six interconnected links that form the vertebrae, with flexible sheets of metal attached to its sides to form a skin [17]. The motion of each link is constrained to pure rotation, and the shape of the vehicle can be controlled by changing the joint angles, via actuators. The metal sheets attached to each link, forming the skin, are independent from each other (they slide with respect to each other) and do not provide significant resistance to link rotation [17]. The rear part of the

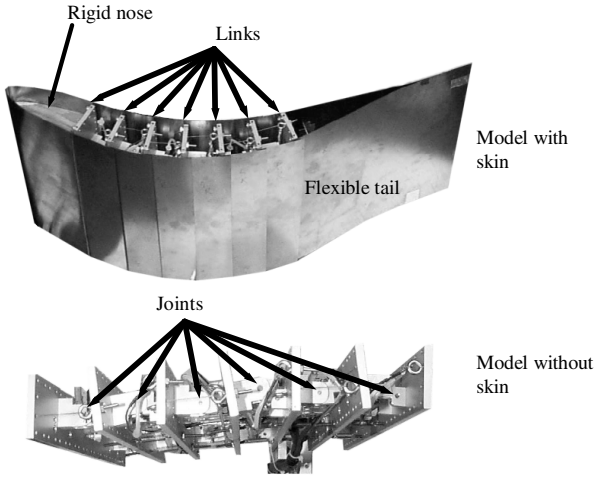

Fig. 1 Reference vehicle from [16].

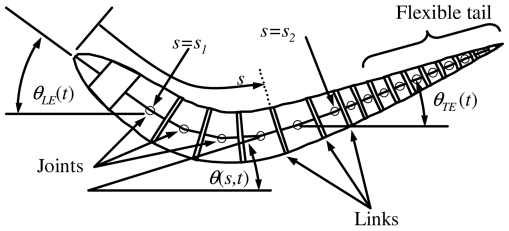

Fig. 2 Model of reference vehicle illustrating vehicle components and geometry of vehicle during a turn maneuver.

model, after the sixth link, has a flexible, nonactuated tail that only responds to inertial and fluid forces (i.e., the tail has no internal actuators).

The mechanical-model features that are reproduced in the present computational model include a backbone made up of joints, body shape controlled by setting the joint angles via internal actuators, a streamlined body, and a flexible tail. These properties are embedded in the geometry of the simulated vehicle, as shown in Fig. 2. The rigid links are interconnected and form the backbone of the vehicle. The flexible tail portion is modeled by a set of 10 smaller rigid links interconnected with torsional dampers and springs to simulate the structural damping and stiffness of the real tail. Because no significant tangential structural forces are transferred by the skin in the mechanical model, the skin in the numerical model did not have axial stiffness and simply served to transfer the normal (pressure) forces from the fluid to the vehicle. The hydrofoil thickness distribution is that of a NACA 0012. The numerical model of the fluid mechanics is based on unsteady inviscid flow, so skin friction effects are not accounted for.

To achieve body deformations and have a sufficiently smooth skin, the surface is defined by fitting a skin over the interconnected links. The skin is created using two spline fits around the ends of the links. The spline fits are created with the horizontal and vertical coordinates as a function of the distance along the vehicle surface from the trailing edge (TE) to the LE and back to the TE around the vehicle. The result is a smooth skin that, as the angles of the links change, stretches or shrinks to conform to the body of the vehicle. Using this technique, all the possible vehicle deformations are attainable by changing the link angles only and not the thickness of each link. The model also includes mass and inertia for each link. This information is needed for the integration of the accelerations into displacements and rotations as the vehicle moves in the fluid. These properties are discussed further in the dynamics section.

Maneuvers

The mechanical model that is the basis for the computational model ideally is capable of maneuvers similar to those of a fish. For the vehicle to perform a turn, it needs to flex its body. A typical profile [8] during a turn maneuver is shown in Fig. 2. The angles of the links during this turn maneuver smoothly vary from θ_{LE} to θ_{TE} between two points on the vehicle (s_1 to s_2 in Fig. 2). The link angle from the leading edge to s_1 is θ_{LE} and the link angles from s_2 to the trailing edge are determined by the dynamic response of the flexible tail. The smooth variation of joint angles between s_1 and s_2 is modeled using a fifth-order ramp shown in Eq. (1) to prevent any kinks in the motion, which in turn prevents problems to the flow solver.

$$\theta(s,t) = \theta_{\mathrm{LE}}(t) + [\theta_{\mathrm{TE}}(t) - \theta_{\mathrm{LE}}(t)] \cdot \left[10 - 15 \cdot \left(\frac{s-s_1}{s_2-s_1}\right) + 6 \cdot \left(\frac{s-s_1}{s_2-s_1}\right)^2\right] \cdot \left(\frac{s-s_1}{s_2-s_1}\right)^3 \quad (1)$$

The second maneuver considered is a fast start. This maneuver is heavily dependent on the properties of the flexible tail properties such as the damping and spring constants used. This type of maneuver is similar to a turn where the vehicle abruptly flexes its body (its first six joints) and then rapidly straightens it. This is similar to the observations made by Beddow et al. [9]. During this motion, the flexible tail would deflect due to inertial and fluid loads. The amount of flexing also depends on the damping and spring constants.

Flow Solver

To provide a theoretical model of the two-dimensional vehicle hydrodynamics, an unsteady potential panel code was developed. The general approach taken is similar to that used by Basu and Hancock [18], properly modified to incorporate a moving body through the fluid as well as body deformations. A detailed description and validation of the flow solver is given in [2,3].

Vehicle Dynamics

The dynamics part of the vehicle simulation contains three sections. The whole vehicle dynamics due to the external loads, the dynamics of the actuated link joints 1–6, and the response of the free tail, which is modeled by a set of 10 links interconnected with springs and dampers.

Whole Vehicle State

The motion of the vehicle is a direct response to the presence of pressure loads on its surface. Vehicle accelerations are directly derived from the fluid loads. First-order Euler integration [19] of the rotational and linear accelerations is used to obtain the vehicle angular and linear velocities first. Then a second integration produces the current rotation and position of the vehicle in the inertial frame. These steps are shown in Eqs. (2–5) where the variables are defined in Fig. 3 and in the nomenclature.

$$\boldsymbol{V}_{ok+1} = \boldsymbol{V}_{ok} + \frac{\boldsymbol{F}_k}{m} \cdot \Delta t \quad (2)$$

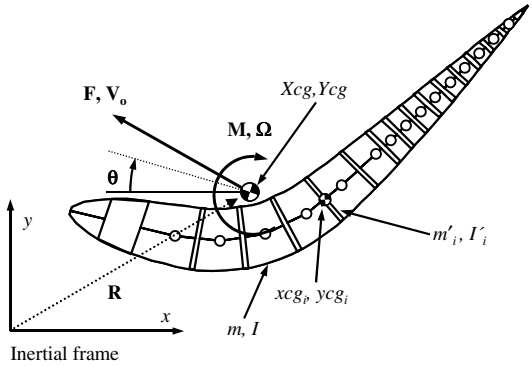

Fig. 3 Definition of variables used in whole vehicle dynamics and calculation of the overall center of mass.

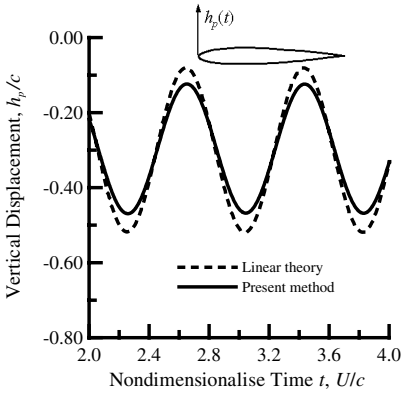

Fig. 4 Validation of the whole vehicle dynamics model against linear theory.

$$\boldsymbol{\Omega}_{k+1} = \boldsymbol{\Omega}_k + \frac{\boldsymbol{M}_k}{I} \cdot \Delta t \tag{3}$$

$$\boldsymbol{R}_{k+1} = \boldsymbol{R}_k + \boldsymbol{V}_{ok} \cdot \Delta t \tag{4}$$

$$\theta_{k+1} = \theta_k + |\boldsymbol{\Omega}_k| \cdot \Delta t \tag{5}$$

Higher-order explicit methods such as the Adams–Bashford [19] three-point integration were tested but did not provide any significant accuracy improvements and tended to be unstable in a few cases where load changes are relatively small or zero. The first-order Euler method proved to be very reliable and insensitive to small load fluctuations produced by the discrete vortices introduced into the wake. Implicit methods were not used because they made the iterative part of the computational procedure intractable and increased the computing time by at least threefold.

As the vehicle deforms, or the links rotate with respect to each other, the center of mass position changes with time. This is relevant, because, for example, the center of mass is used as the basis for the calculation of the moment $\boldsymbol{M}$. The horizontal and vertical positions of the center of mass of the vehicle are given by Eqs. (6) and (7) where the individual link masses and positions are defined, as shown in Fig. 3.

$$Xcg = \frac{\sum_{i=1}^{N} xcg_i \cdot m_i'}{m} \tag{6}$$

$$Ycg = \frac{\sum_{i=1}^{N} ycg_i \cdot m_i'}{m} \tag{7}$$

The masses and centers of mass of the individual links are considered constant. As a validation case, a rigid NACA 0012 airfoil free to move in plunge is pitched about its quarter chord. The free plunge response of the airfoil calculated with the present dynamics integration method is compared with Theodorsen's linear theory [20]. This comparison is presented in Fig. 4. The linear theory predicts a slightly larger displacement than the present method but the phase information is matched. The discrepancies are present because the linear theory does not account for vehicle thickness or a highly curved wake.

Loads on Controlled Joints

The forward six links are interconnected with torsional actuators and one of the goals is to determine the needed torques of these actuators so that the vehicle deforms as required. The Featherstone algorithm [21] is used to calculate the unknown torques. This procedure relates the link dynamics and the loads acting on each link. The setup needed for this method is shown in Fig. 5, where the links are idealized as interconnected rigid members and only a close-up of three consecutive links is considered for discussion. The top schematic of Fig. 5 shows the kinematic and geometric definitions, whereas the bottom schematic shows the loads acting on each link as well as the reactions at the joints. The Featherstone algorithm can be used to find these reactions and thus the needed torque at each joint. This method can be summarized in Eqs. (8–10) where a dot indicates differentiation with respect to time.

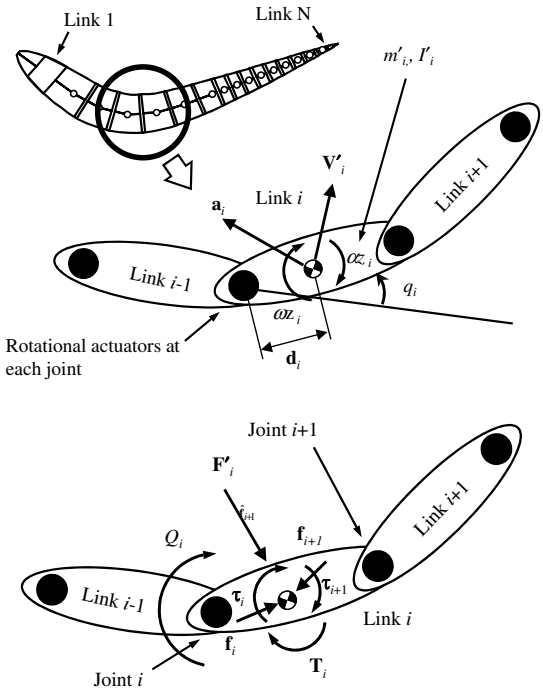

Fig. 5 Kinematic properties of each link and loads acting on each actuated link.

$$\hat{\boldsymbol{a}}_i = \begin{Bmatrix} \boldsymbol{\alpha}_i \\ \boldsymbol{a}_i \end{Bmatrix} = B1 \cdot \hat{\boldsymbol{a}}_{i-1} + \ddot{q}_i \cdot \hat{\boldsymbol{d}}_i + \hat{\boldsymbol{C}}_i \tag{8}$$

$$\hat{\boldsymbol{f}}_i = \boldsymbol{m}_i \cdot \hat{\boldsymbol{a}}_i + \hat{\boldsymbol{F}}_i + B2 \cdot \hat{\boldsymbol{f}}_{i+1} \tag{9}$$

$$Q_i = \hat{\boldsymbol{s}}_i \cdot \hat{\boldsymbol{f}}_i \tag{10}$$

The acceleration equation is given by Eq. (8). The calculation of the link accelerations starts at the TE of the vehicle, where $i = N$, and marches toward the LE where $i = 1$ (Fig. 5). The acceleration of the joint is given by $\ddot{q} \cdot \mathbf{d}$ and the Coriolis terms are in $\mathbf{C}_i$. The deflection information is fed into this expression by using q. The acceleration vector given by Eq. (8) can be written in detailed form as shown in Eq. (16) where i is the index for the link starting at the LE of the vehicle. Because the present problem is two-dimensional, the following equations hold:

$$\boldsymbol{\alpha} = \begin{pmatrix} 0 & 0 & \alpha z \end{pmatrix}^T \tag{11}$$

$$\boldsymbol{a} = \begin{pmatrix} ax & ay & 0 \end{pmatrix}^T \tag{12}$$

$$\boldsymbol{\Omega} = \begin{pmatrix} 0 & 0 & \omega z \end{pmatrix}^T \tag{13}$$

$$\boldsymbol{r} = \begin{pmatrix} rx & ry & 0 \end{pmatrix}^T \tag{14}$$

$$\hat{\boldsymbol{d}} = \begin{pmatrix} 0 & 0 & 1 & -dy & dx & 0 \end{pmatrix}^T \tag{15}$$

$$\begin{pmatrix} 0 \\ 0 \\ \alpha z_{i,k} \\ a x_{i,k} \\ a y_{i,k} \\ 0 \end{pmatrix} = \begin{bmatrix} 1 & 0 & 0 & 0 & 0 & 0 \\ 0 & 1 & 0 & 0 & 0 & 0 \\ 0 & 0 & 1 & 0 & 0 & 0 \\ 0 & 0 & -ry_{i,k} & 1 & 0 & 0 \\ 0 & 0 & rx_{i,k} & 0 & 1 & 0 \\ ry_{i,k} & -rx_{i,k} & 0 & 0 & 0 & 1 \end{bmatrix} \cdot \begin{pmatrix} 0 \\ 0 \\ \alpha z_{i-1,k} \\ a x_{i-1,k} \\ a y_{i-1,k} \\ 0 \end{pmatrix} + \ddot{q}_{i,k} \cdot \begin{pmatrix} 0 \\ 0 \\ 1 \\ -dy_{i,k} \\ dx_{i,k} \\ 0 \end{pmatrix} + \begin{pmatrix} 0 \\ 0 \\ 0 \\ -(\omega z_{i-1,k})^2 \cdot rx_{i,k} - 2 \cdot \omega z_{i-1,k} \cdot \dot{q}_{i,k} \cdot dx_{i,k} - (\dot{q}_{i,k})^2 \cdot dx_{i,k} \\ -(\omega z_{i-1,k})^2 \cdot ry_{i,k} - 2 \cdot \omega z_{i-1,k} \cdot \dot{q}_{i,k} \cdot dy_{i,k} - (\dot{q}_{i,k})^2 \cdot dy_{i,k} \\ 0 \end{pmatrix} \tag{16}$$

where the angular acceleration of each link is given by

$$\omega z_{i,k} = \omega z_{i-1,k} + \dot{q}_{i,k} \tag{17}$$

Once the acceleration term has been calculated for the entire structure, the joint loads or reactions can be determined using Eq. (9). In this expression, $\hat{\boldsymbol{f}}_{i,k}$ is a vector containing the forces and moments acting on joint i at time t_k referenced to the center of mass of link i. The variable $\hat{\boldsymbol{f}}_{i,k}$ contains the forces and torques acting on the center of mass of link i. Again, because the problem is two-dimensional, the following equations hold:

$$\boldsymbol{F}' = \begin{pmatrix} F'_x & F'_y & 0 \end{pmatrix}^T \tag{18}$$

$$\boldsymbol{T} = \begin{pmatrix} 0 & 0 & T_z \end{pmatrix}^T \tag{19}$$

Using Eqs. (18) and (19), Eq. (9) can be written in detail as Eq. (20), where the first matrix multiplication represents the mass-inertia matrix and acceleration product. The second term represents the external loads, which in this case are the fluid loads, and the last term is the effect of the outboard joint reactions.

$$\begin{pmatrix} fx_{i,k} \\ fy_{i,k} \\ fz_{i,k} \\ \tau x_{i,k} \\ \tau y_{i,k} \\ \tau z_{i,k} \end{pmatrix} = \begin{bmatrix} 0 & 0 & 0 & m'_i & 0 & 0 \\ 0 & 0 & 0 & 0 & m'_i & 0 \\ 0 & 0 & 0 & 0 & 0 & m'_i \\ Ix_i & Ixy_i & Ixz_i & 0 & 0 & 0 \\ Iyx_i & Iy_i & Iyz_i & 0 & 0 & 0 \\ Izx_i & Izy_i & Iz_i & 0 & 0 & 0 \end{bmatrix} \cdot \begin{pmatrix} 0 \\ 0 \\ \alpha z_{i,k} \\ a x_{i,k} \\ a y_{i,k} \\ 0 \end{pmatrix} - \begin{pmatrix} Fx_{i,k} \\ Fy_{i,k} \\ 0 \\ 0 \\ 0 \\ Tz_{i,k} \end{pmatrix} + \begin{bmatrix} 1 & 0 & 0 & 0 & 0 & 0 \\ 0 & 1 & 0 & 0 & 0 & 0 \\ 0 & 0 & 1 & 0 & 0 & 0 \\ 0 & 0 & ry_{i,k} & 1 & 0 & 0 \\ 0 & 0 & -rx_{i,k} & 0 & 1 & 0 \\ -ry_{i,k} & rx_{i,k} & 0 & 0 & 0 & 1 \end{bmatrix} \cdot \begin{pmatrix} fx_{i+1,k} \\ fy_{i+1,k} \\ fz_{i+1,k} \\ \tau x_{i+1,k} \\ \tau y_{i+1,k} \\ \tau z_{i+1,k} \end{pmatrix} \tag{20}$$

To obtain the reactions at a joint location, the loads must be transferred to the joint from the center of mass of the corresponding link. The result of that operation is Eq. (21). This expression provides the desired torque values for joint i at time t_k needed for the vehicle to deform its body as required for a maneuver.

$$Q_{i,k} = \tau z_{i,k} + dx_{i,k} \cdot fy_{i,k} - dy_{i,k} \cdot fx_{i,k} \tag{21}$$

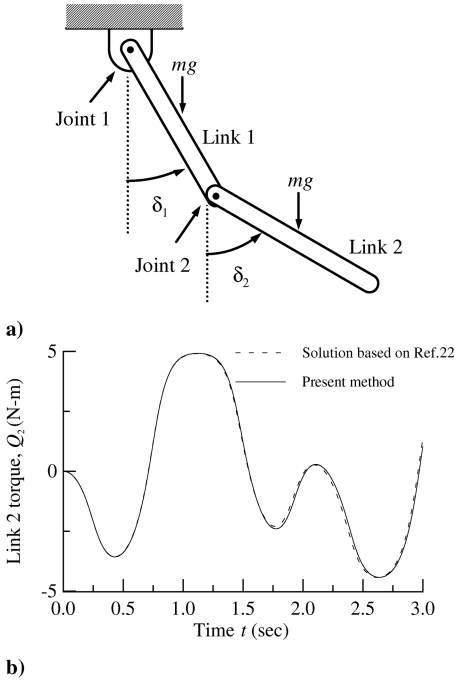

Fig. 6 Compound pendulum a) for dynamics validation and validation of the joint loads against [22], and b) validation of torque loads against [22].

Validation for Joint Torque Calculation Procedure

The validation for the needed torque at a joint was done by comparing the present method to the solution of a compound pendulum [22]. The pendulum is made of two connected bars of mass and length with one of the bars attached to a fixed point as shown in Fig. 6a. The external forces acting on the pendulum are due to the influence of gravity on each bar.

The pendulum problem is composed of two, second-order differential equations [22] and can be solved to determine the bar angles. The goal of the validation is, given the time history of the angles δ_1 and δ_2 for specific initial conditions, to determine the equivalent torques at each joint so that the pendulum follows the specified time history of δ_1 and δ_2. The simulation is started with the pendulum at rest with $\delta_1 = 45$ deg and $\delta_2 = 0$ deg using a time step of 0.0025 s. Then the moments acting on the joints and the bar angles were extracted from the solution. The angles were used by the present method to find the required moments at the joints needed for the bars to follow the given angles. The results are given in Fig. 6b. The moment acting on joint two, according to [22], is a direct function of the link angles and link properties. There is good agreement between the exact and the calculated torques. The small discrepancies may be present because Euler integration is used in the present method.

Flexible Tail Dynamics

The flexible tail of the model responds to the fluid, inertial, and structural loads but there is no direct actuation/control of its link angles. The goal of the simulation of the free-tail section of the model is to calculate the deformation of the tail as the flow, the inertia, and the inner springs and dampers affect the structure. This offers a swimming and maneuvering optimization tool. In other words, it can be used to design the optimal structural properties of the flexible tail in order for certain swimming or maneuvering criteria to be met, such as maximum energy efficiency, maximum starting-from-rest acceleration, and minimum turning radius. A detailed schematic of

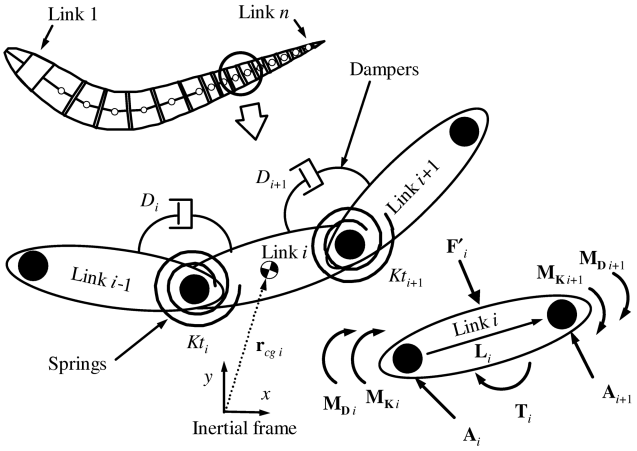

Fig. 7 Details of flexible tail model.

three consecutive links is shown in Fig. 7 where the dampers and springs act at the joints. The dampers simulate the structural damping and the springs the structural stiffness. One link is shown with all the forces and moments that act on it. The basic relations that apply to each link in this setup are

$$\boldsymbol{\alpha}_{i,k} = \frac{\sum \boldsymbol{M}_{\mathbf{joint}\,i,k}}{I_i} \tag{22}$$

$$\boldsymbol{\omega}_{i,k+1} = \boldsymbol{\omega}_{i,k} + \boldsymbol{\alpha}_{i,k} \cdot \Delta t \tag{23}$$

$$\theta_{i,k+1} = \theta_{i,k} + |\boldsymbol{\omega}_{i,k}| \cdot \Delta t \tag{24}$$

where $\boldsymbol{M}_{\mathbf{joint}\,i,k}$ is the sum of the moments due to the fluid, springs, dampers, and reactions for link i about joint i at time t_k. Once the angles are determined, the shape of the tail can be calculated easily starting from the tail tip. The moments acting on each link in the tail are described by Eqs. (25–31) where the k index has been dropped for simplicity, and the variables used are described in Fig. 7.

$$\boldsymbol{M}_{\boldsymbol{K}i} = -(\boldsymbol{\theta}_i - \boldsymbol{\theta}_{i-1}) \cdot Kt_i \tag{25}$$

$$\boldsymbol{M}_{\boldsymbol{K}i+1} = -(\boldsymbol{\theta}_i - \boldsymbol{\theta}_{i+1}) \cdot Kt_{i+1} \tag{26}$$

$$\boldsymbol{M}_{\boldsymbol{D}i} = -(\boldsymbol{\omega}_i - \boldsymbol{\omega}_{i-1}) \cdot D_i \tag{27}$$

$$\boldsymbol{M}_{\boldsymbol{D}i+1} = -(\boldsymbol{\omega}_i - \boldsymbol{\omega}_{i+1}) \cdot D_{i+1} \tag{28}$$

$$\boldsymbol{M}_{\boldsymbol{A}i} = 0 \times \boldsymbol{A}_i = 0 \tag{29}$$

$$\boldsymbol{M}_{\boldsymbol{A}i+1} = \boldsymbol{L}_i \times \boldsymbol{A}_{i+1} \tag{30}$$

$$\sum \boldsymbol{M}_{\text{joint}i} = \boldsymbol{M}_{\boldsymbol{K}i} + \boldsymbol{M}_{\boldsymbol{K}i+1} + \boldsymbol{M}_{\boldsymbol{D}i} + \boldsymbol{M}_{\boldsymbol{D}i+1}\boldsymbol{M}_{\boldsymbol{A}i+1} \tag{31}$$

Once the joint moment has been determined, the angles can be integrated for that time using Eqs. (22–24) and the entire process is repeated for the next iteration. The reaction forces are calculated by using Newton's second law on each link. The link acceleration is

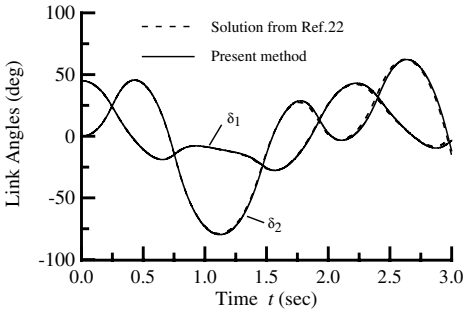

Fig. 8 Validation of the tail dynamics procedure against [22].

calculated first by using the position history of the link in space. The entire process starts at the TE link (where $i = n$), because the outboard reaction ($\boldsymbol{A}_{n+1}$) would be zero at that location, and then marches toward the tail root. The procedure to calculate the reactions is shown in Eqs. (32–34).

$$\boldsymbol{a}_i = \Delta \boldsymbol{r}_{cgi}/\Delta t \tag{32}$$

$$\sum \boldsymbol{F}_{\text{link}i} = \boldsymbol{A}_i + \boldsymbol{F}'_{\mathbf{i}} + \boldsymbol{A}_{i+1} = m'_i \cdot \boldsymbol{a}_i \tag{33}$$

$$\boldsymbol{A}_i = m'_i \cdot \boldsymbol{a}_i - \boldsymbol{F}'_{\mathbf{i}} - \boldsymbol{A}_{i+1} \tag{34}$$

Note that the simulation time step is the same as for the flow solver and care must be applied as to how to account for the fluid-structure interaction. A proposed method [23] to accomplish proper fluid-structure interaction is to follow these steps: 1) integrate position and/or tail dynamics (structure), 2) calculate surface movement, 3) call flow solver and calculate loads, and 4) update structure to t_{k+1} with the fluid loads.

Flexible Tail Dynamics Validation

The validation of the flexible tail dynamics was done using the same pendulum approach as for the torque validation mentioned earlier. In this case, the goal is to predict the pendulum deflection angles from the torques applied to the pendulum from gravity in this case. Gravity acts on each pendulum bar similarly to the fluid, spring, and external forces on the vehicle tail links. Using the known torque at each joint from the pendulum solution the present method was used to predict the bar angles. These results were compared with the exact solution from [22], as shown in Fig. 8. The small discrepancies are present due to the Euler integration used.

Vehicle Control

In order for the simulation vehicle to navigate a given set of waypoints autonomously, a general relation among body deflections, flow conditions, vehicle motions, and desired trajectory must be determined. The needed control is divided into two tasks. One is the determination of the required turning maneuvers for the vehicle to follow a prescribed path. The other is the acceleration maneuvers needed for the vehicle to keep a required velocity or time schedule while navigating.

Navigation Control

The layout of the vehicle, as it travels a given path made up of waypoints, is given in Fig. 9. The path is formed by linear interpolation through the x and y coordinates of the waypoints. From this path description the input variables can be preliminarily identified. The known information at time $t = t_i$ includes body pitch, TE root angle deflection, velocity magnitude, and current vehicle position, along with their history at $t = t_{i-1}$, t_{i-2}, and earlier. The known information at $t = t_{i+1}$ is the desired vehicle position

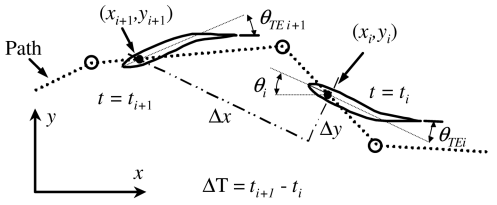

Fig. 9 Geometric parameters during navigation.

(x_{i+1}, y_{i+1}) at that time. All the given waypoint positions are also known. The vehicle changes direction by flexing its tail, and so at $t = t_i$ the only needed information is the amount that the trailing edge should be deflected ($\theta_{\text{TEroot}\,i+1} - \theta_{\text{TEroot}\,i}$) so that the vehicle follows the path by reaching (x_{i+1}, y_{i+1}). The tail angle is changed by deflecting body links 1–6.

From this information, the control problem can be simplified into a prediction procedure where the required output is $\theta_{\text{TEroot}\,i+1}$ and the input would be composed of some or all of the known properties previously listed. In other words, the trailing edge root deflection $\theta_{\text{TEroot}\,i+1}$ can at most depend on the following list of variables:

$$\theta_{\text{TEroot}\,i+1} = f(x_{i+1}, x_i, x_{i-1}, \ldots, y_{i+1}, y_i, y_{i-1}, \ldots, V_i, V_{i-1}, \ldots, \theta_{\text{TEroot}\,i}, \theta_{\text{TEroot}\,i-1}, \ldots, \theta_i, \theta_{i-1}, \ldots) \tag{35}$$

However, by investigating the effect of the input variables on the output variable ($\theta_{\text{TEroot}\,i+1}$), significant order reduction can be achieved with negligible effect on the accuracy of the model. The reader is also referred to Galls and Rediniotis [2], where a similar order-reduction procedure was followed for the case of a rigid tail. To this end, many training cases are executed using the panel code simulation described earlier. These cases are created by deflecting the trailing edge root through a range of different schedules that are designed to check for relationships between the input variables and the output.

A typical TE root deflection schedule is shown in Fig. 10. The deflection is varied between −60 and +60 deg with each case having three distinct TE root angle variations. The root angle values $\theta_{\text{TEroot}\,i-1}$, $\theta_{\text{TEroot}\,i}$, and $\theta_{\text{TEroot}\,i+1}$ are varied from −60 to +60 deg in 20 deg increments, resulting in 216 cases that were executed using the unsteady potential code. For example, the hydrofoil would start undeformed at $t = 0$ s and could then be commanded to ramp up to a TE root deflection of 10 deg in time ΔT_4, then go to 20 deg ΔT_4 later, and then −10 deg ΔT_3 later. For these tests, 40 panels are used on the vehicle surface and the time step is 0.0025 s. To be useful in this analysis, the x_{i+1} and y_{i+1} positions of the vehicle are converted to relative positions with respect to the current position of the vehicle and then expressed in local vehicle axes as seen in Fig. 9. Also Δx and Δy are normalized by $V \cdot \Delta T$.

$$\overline{\Delta x} = \frac{\Delta x}{V \cdot \Delta T}, \qquad \overline{\Delta y} = \frac{\Delta y}{V \cdot \Delta T} \tag{36}$$

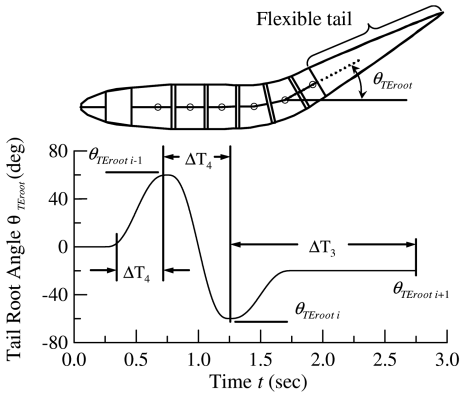

Fig. 10 Tail deflection history for navigation training.

By analyzing the data from the training cases, it was observed that the variation of $\overline{\Delta x}$ is relatively small compared with the variation of $\overline{\Delta y}$, and so $\overline{\Delta x}$ can be dropped from the input list. Because body pitch is the orientation of the vehicle in the inertial frame, a more insightful variable would be the relative pitch change from the previous position to the current one:

$$\Delta\theta = \theta_i - \theta_{i-1} \tag{37}$$

As it is also discussed in [2], a way to include the history of the trailing edge root angle is to define a variable that would capture the rate of TE root angle deflection and scale it with the velocity and the chord of the vehicle. This quantity is defined as

$$K_{\text{root}} = \frac{(\theta_{\text{TEroot}\,i} - \theta_{\text{TEroot}\,i-1}) \cdot c}{V \cdot \Delta T_4} \tag{38}$$

where the time interval ΔT_4 is fixed and is defined as shown in Fig. 10. Essentially, K_{root} is the nondimensional angular deflection rate of the trailing edge root. Taking into consideration the previous arguments, the TE root angle at $t = t_{i+1}$ can be predicted using the simplified relation shown in Eq. (39).

$$\theta_{\text{TEroot}\,i+1} = f(\theta_{\text{TEroot}\,i}, K_{\text{root}}, \overline{\Delta y}, \Delta\theta) \tag{39}$$

Comparing the inputs, it was found that the body pitch change and the tail root angle $\theta_{\text{TEroot}\,i+1}$ are closely related while using the flexible tail and it was considered to be a linear relationship as shown in Fig. 11. Therefore, one of the variables can be dropped from the set of input variables. The resulting inputs and output are as shown in Eq. (40):

$$\theta_{\text{TEroot}\,i+1} = f(\theta_{\text{TEroot}\,i}, K_{\text{root}}, \overline{\Delta y}) \tag{40}$$

This is a relation with three inputs and one output and can be easily trained in an artificial neural network setup. This model uses a feed-forward network, trained through back-propagation. The first and second layers use a hyperbolic tangent sigmoid transfer function and the last layer uses a linear transfer function. It was discovered that more layers/nodes per layer or data from points older than $t = t_{i-1}$ do not improve prediction accuracy. The resulting artificial neural network can predict back the training data with an error of less than 3 deg. The procedure used for obtaining the tail root angle is the same as for the rigid tail described in [2]. If the prediction is performed at intervals of $\Delta T = \Delta T_3$ (1.5 s), the procedure was accurate but the vehicle would oscillate about the path. Because sampling can be performed at intervals of anything from ΔT_4 to ΔT_3, sampling the path at a faster rate, such as at intervals of $\Delta T = \Delta T_4$ (0.5 s), eliminated this overprediction.

As expected, the mass and inertia about the center of mass affect the behavior of the vehicle during a TE maneuver. Larger mass values make the velocity magnitude and direction of the vehicle less sensitive to changes in body deflections. Likewise, as the mass is decreased, the velocity of the vehicle becomes more responsive to body deformations to the point of almost being unstable during the simulation. Similarly, increasing and decreasing the inertia of the vehicle correspondingly decreased and increased the rotational velocity sensitivity to body deformations. As the inertia decreases, the turning radius of the vehicle, while the TE is locked into a fixed deflection, also decreases. Positioning of the center of mass is also critical to the performance of the vehicle. Placing the center of mass close to the LE makes the vehicle very stable. In this case, large tail deflections are required for proper control. If the center of mass is located further away from the LE, the vehicle becomes unstable, especially if the center of mass is located behind the hydrodynamic center. The goal is to set a realistic mass, center of mass, and inertia that would provide a maneuverable vehicle without making it unstable. The mass and inertia about the center of mass of the vehicle were set at 10.0 Kg and 0.5 $\text{N} \cdot \text{m/s}^2$, respectively, with the center of mass at 12% of the chord from the LE, which correspond closely to the configuration of the reference vehicle [17].

Acceleration Control

As mentioned in [9], acceleration can be performed via a fast start maneuver, as encountered in fish. In this maneuver, the fish performs a quick tail beat cycle and then coasts. This is typical of many fish and is often referred to as burst-coast swimming. The advantage of this type of swimming is that it requires less body motion compared with continuous-stroke swimming. In the case of an underwater vehicle, this feature can be of great value to conserving energy. Because of this, the burst-coast type of acceleration is chosen for the current vehicle.

The vehicle deformations needed for a change of velocity (ΔV) can be described as shown in Eq. (41). Here, θ_1–θ_n represent the angles of the vehicle links as a function of time during the acceleration maneuver from $t = t1$ to $t = t2$ where $\Delta Ta = t2 - t1$. In this case, it is assumed that the change in velocity is determined for a time sufficiently large for the vehicle to have reached a steady velocity. Because of these assumptions, only the change in velocity, its magnitude and time it took to accelerate are useful. Histories of the vehicle parameters such as previous velocity, pitch rate, or vehicle pitch are not considered because at the end of the maneuver the vehicle is close to steady motion.

$$\theta_i(t) = f_i(\Delta V, V, \Delta Ta), \qquad i = 1, \ldots, n \tag{41}$$

If the vehicle would deform its body by performing a maneuver similar to that of a fast start [9], the link angles can be defined by a function that is controlled by a few parameters and Eq. (41) can be greatly simplified. The acceleration maneuver was then chosen as a turning maneuver modified to resemble a C-start. The C-start is more suited to the present vehicle design because the tail is not directly controlled and most of the deformation is obtained by the body of the fish [9] (successive stages of a C-start were also tested). The modified fast start maneuver sequence for the tail root angle is $+\theta_{\max}$, $-\theta_{\max}$, $+\theta_{\max}/2$, and finally to zero in a time lapse of ΔTa. The maneuver is designed such that when the maneuver is completed, the vehicle would keep an orientation close to what it had before it started the maneuver. This is to avoid extra energy wasted in trying to reorient the vehicle every time it accelerates. The resulting output is $\theta_{\max}$ and the inputs are reduced to ΔV, V, and ΔTa. It is discovered that ΔTa could be left constant and the final version of the function that needs to be encoded by the artificial neural network is shown in Eq. (42):

$$\theta_{\max} = h(\Delta V, V) \tag{42}$$

The parameters in Eq. (42) are varied and a process similar to the navigation training is performed. A typical test is shown in Fig. 12. The value of ΔTa is fixed at 2.0 s. The values of $\theta_{\max}$ are varied from 20 to 80 deg in 20 deg increments. The values of the starting velocity are varied from 0.12 to 1.67 body lengths/s at about 0.82 body lengths/s increments. The collected results for the velocity change for different cases of $\theta_{\max}$ and V are shown in Fig. 13. It is noted that for the same $\theta_{\max}$ the change in velocity decreased with

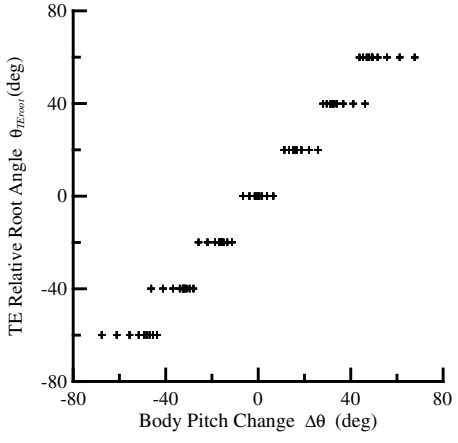

Fig. 11 Relation between body pitch angle and TE root angle.

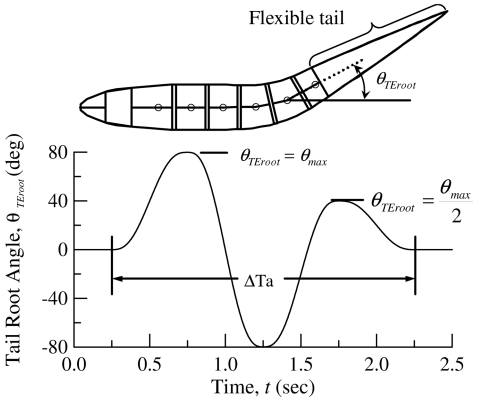

Fig. 12 Tail deflection history for acceleration training.

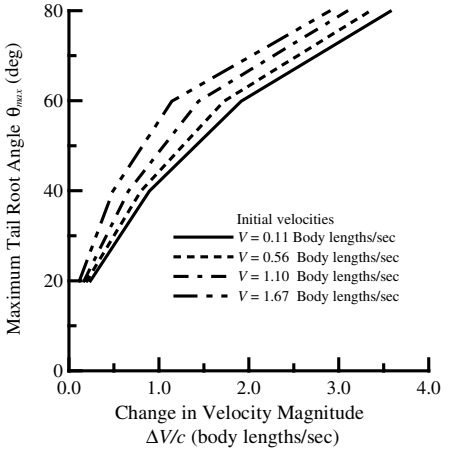

Fig. 13 Values of acceleration maneuver parameter for different input values of ΔV and V.

increasing V. This indicated a limit on how much extra velocity the vehicle can generate for a given $\theta_{\max}$ and ΔTa, and that after some limiting value of V there would be no further acceleration. A simple artificial neural network is used to predict $\theta_{\max}$ from the inputs with an error of less than 0.1%. The network uses three layers, where the first and second layers use a hyperbolic tangent sigmoid transfer function. The last layer uses a linear transfer function. The prediction procedure is as follows:

1) At $t = t_i$, calculate the change in velocity needed from the current velocity.

2) Determine $\theta_{\max}$ using the inputs in step 1 and the artificial neural network.

3) Deflect the tail root as indicated in Fig. 12 from $t = t_i$ to $t = t_i + \Delta Ta$.

4) Advance the time instant and return to step 1.

Results and Discussion

Navigation

These tests were performed using 40 panels and a time step of 0.0025 s. The starting velocity for all the tests is about 1.14 chords/s. Case 1, shown in Fig. 14, is designed to test the trajectory following of the vehicle and the sampling time sensitivity. If the sampling of the trajectory is performed every 0.5 s, the path is closely followed. On the other hand, if the sampling occurs every 1.5 s (or ΔT_3), the oscillations about the path are large (Fig. 14a). In both cases, the simulation ran for the same time and the case using the slower sampling moved so far from the path that it lagged behind the case for the faster sampling.

The tail root angle deflection for case 1 is shown in Fig. 14b. Here, it can be clearly seen that the deflection needed for the faster sampling ($\Delta T = \Delta T_4 = 0.5$ s) is significantly less than that for the slower

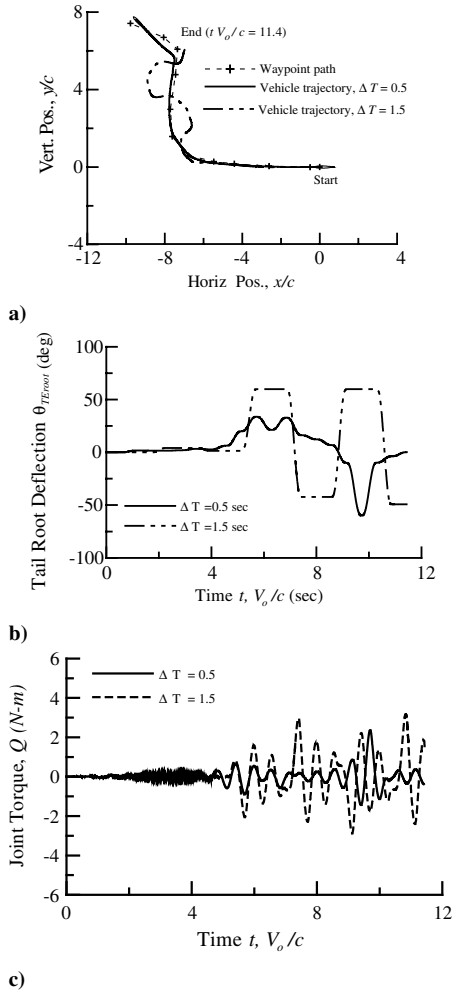

Fig. 14 Vehicle response for navigation case 1: a) vehicle trajectory, b) tail root deflection history, and c) joint six actuator torque.

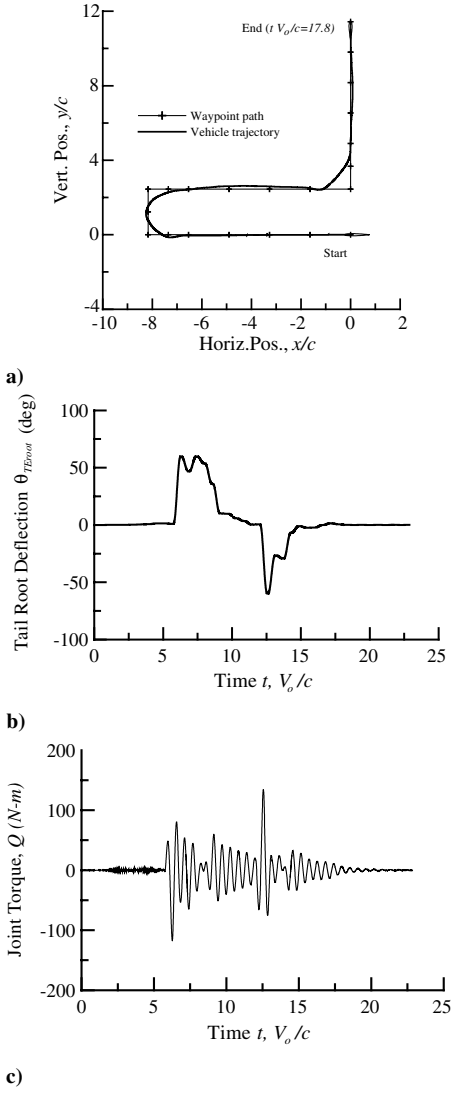

Fig. 15 Vehicle response for navigation case 2: (a) vehicle trajectory, (b) tail root deflection history, (c) joint 6 actuator torque.

sampling. Other advantages are that the predictions do not run into the limits of the tail deflection range at ± 60 deg and that the tail root deflection rates are much lower for the faster sampling. This is also shown in Fig. 14c, in which the needed torque for joint actuator six in case 1 is presented. The rest of the actuators have similar behavior. The maximum torque needed for slower sampling is about 25% greater than for fast sampling. The power needed is also less, which is indicated by the typically smaller rates at which the actuators should operate. Also, the energy used, which is related to the integral of the torque, is less.

Case 2 is shown in Fig. 15 and it shows how the vehicle can turn at different speeds and follow a trajectory after a strong tail deflection. As the trajectory is followed, the speed of the vehicle does increase because of the flexible tail acting on the flow. In the flexible tail case, as the vehicle reaches the last turn, there is no overshoot of the desired trajectory. A salient feature of this test is the turning performance change. As the third turn is reached, the vehicle starts turning earlier (Fig. 15a). This occurs because the speed of the vehicle has increased due to the flexible tail interacting with the flow. Every turn adds some speed to the vehicle and the prediction method must adjust the procedure for the change. As the speed increases, the further the distance that the navigation procedure must "look ahead" and thus the turning starts earlier, so that the vehicle does not overshoot the corner. At this point, the distance ahead that the search procedure uses is about 2.45 body lengths in front of the vehicle, so that the turning maneuver starts early resulting in the vehicle aligning itself quickly with the trajectory after the turn. Also, this test shows how the vehicle can keep on a straight track without diverging. The tail root deflection history for case 2 is shown in Fig. 15b. The deflections are confined to the turns only and the deflections during the straight segments are small. The torque at joint six for case 2 is shown in Fig. 15c. One feature that can be seen there is that, even during the straight paths of the trajectory, after the vehicle has performed a turn, the actuators still need to develop nonzero torques to properly react to the free response of the tail. As the flexible tail deflects under the influence of fluid-structure interaction, it forces the actuators to act accordingly to maintain the commanded/desired vehicle shape. This effect, as with the simple spring-mass system, decreases with time once the tail root stops moving. As the vehicle travels the last straight segment ($t > 12$ s) the torques decrease rapidly with time.

Case 3, shown in Fig. 16, is an extreme case where the vehicle is forced to turn on itself. The vehicle starts at $x/c = 0$, $y/c = 0$, and moves on a straight line along the negative x axis to $x/c = -3.27$ at which point it starts its turning. When it completes its maneuver, it is moving along the positive x axis at $y/c = 0$. Once the vehicle reaches $x/c = -3.27$, it starts deflecting the tail root until it reaches the limit during navigation of 60 deg (Fig. 16a). This can be seen in the tail root deflection history in Fig. 16b. There is a gradual deflection at first and then it rapidly reaches the limit. Once the vehicle is starting to align with the trajectory, the tail root is gradually brought back toward zero and then quickly turned the other way for the final adjustment to stay on the path. As in the previous cases, the joint torques oscillate due to the tail flexibility as shown in Fig. 16c. Because of the damping present in the flexible tail, the oscillations last only a few seconds.

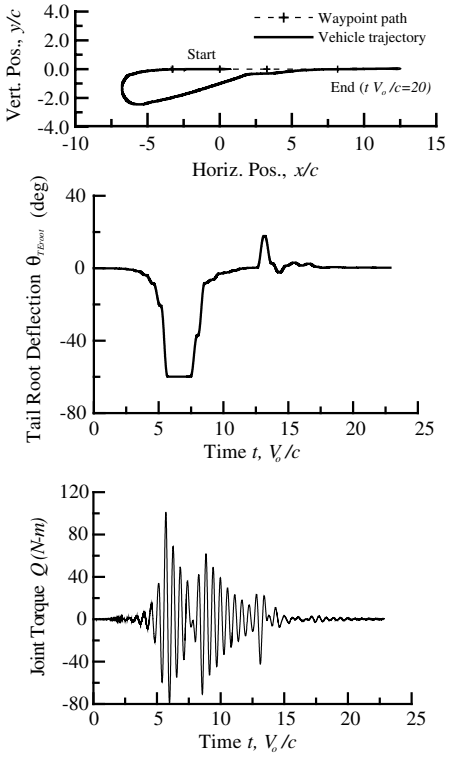

Fig. 16 Vehicle response for navigation case 3: a) vehicle trajectory, b) tail root deflection history, and c) joint six actuator torque.

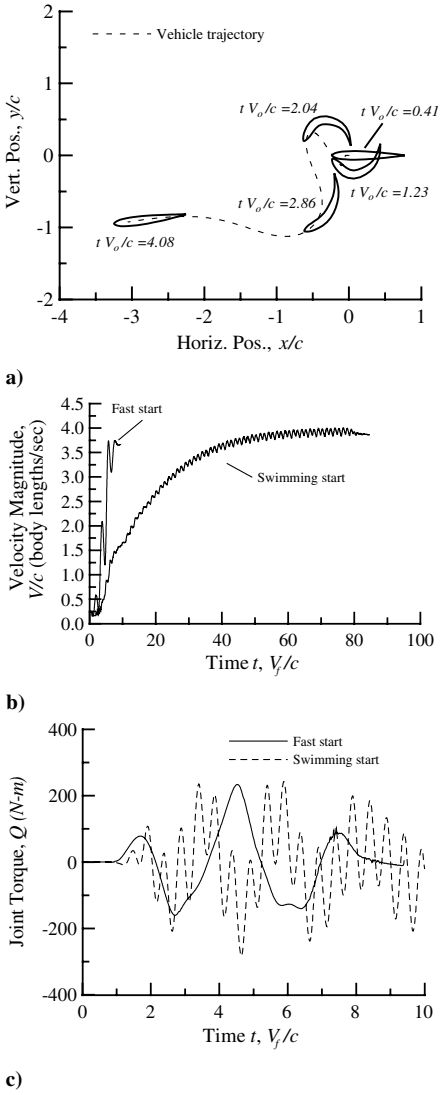

Fig. 17 Vehicle response for acceleration case 1: a) vehicle profile history, b) vehicle velocity profile, and c) joint six actuator torque.

Acceleration

There two cases shown. Both cases have an initial velocity in the negative x direction and the vehicle starts aligned with the negative x axis. Case 1, shown in Fig. 17, started with the vehicle at an initial velocity of 0.11 body lengths/s. The vehicle profile for this case is shown at different times in Fig. 17a. In the fast start procedure shown in Fig. 17, the maximum tail deflection was set to $\theta_{\max} = 80$ deg. The tail root is flexed to $\theta_{\max}$ at 0.75 s and then rapidly deflected to $-\theta_{\max}$ at 1.25 s. The vehicle does not show any significant displacement until the tail root moves from $\theta_{\max}$ to $-\theta_{\max}$. During this period, the vehicle does experience a significant change in pitch to the point of being placed almost perpendicular to its original direction. To rotate the vehicle back to its original direction, the tail root is deflected back to $\theta_{\max}/2$. The velocity profile is shown in Fig. 17b. The velocity profile for a swimming start, where the vehicle is continually oscillated until it reaches a steady velocity, is also shown. The final velocity at 2.25 s (the end of the fast start maneuver) is 3.76 body lengths/s resulting in an acceleration of about 1.83 body lengths/s^2. The fast start reaches the steady velocity in about one-eighth of the time it takes for the swimming start. The time lapse for the maneuver is fixed at $\Delta Ta = 2.0$ s. The required torque at joint six for case 1 is shown in Fig. 17c. The actuation has much lower time gradients for the fast start and thus requires less power than the swimming start.

Case 2 is a combination of navigation and acceleration maneuvers. The vehicle path for this case is shown in Fig. 18a. The acceleration starts at $t = 5$ s and lasts for 2 s. By the time the vehicle reaches the left upper corner in Fig. 18a, its speed is about 2.12 body lengths/s as shown in the velocity profile in Fig. 18b. The velocity does change significantly with every turn, as was mentioned earlier. The tail root angle history is shown in Fig. 18c. The acceleration maneuver is marked and clearly follows what is shown in Fig. 18a. One thing to notice in Fig. 18a is that after the acceleration maneuver, the vehicle is able to return to the trajectory. That is why, after the acceleration response of the body pitch, it is important to have the vehicle in a general direction similar to that before the acceleration. This allows the navigation procedure to quickly recover the vehicle from any divergence produced by the acceleration maneuver.

Conclusions

Navigation and acceleration control for a biomimetic underwater vehicle were simulated using an unsteady flow solver incorporating the vehicle dynamics and an artificial neural network. The vehicle features a multivertebra spine and a flexible tail. An unsteady panel method was used to generate the hydrodynamic load data so that the most important parameters for navigation and acceleration can be identified. By combining the vehicle, spine, and tail dynamics into the unsteady flow solver, the resulting vehicle positions and changes in velocity due to numerous deflection schedules were calculated. The results were examined, and the important geometric and flow variables were identified and properly scaled. The list of conclusions is as follows:

1) The comparison of input and output variables allowed for a significant model order reduction. Subsequently, the reduced data were used to train the artificial neural network for both navigation and acceleration.

2) The network input was a set of geometric and state variables, and the network predicted the needed body/spine deformations so that the vehicle may navigate or accelerate through a set of given waypoints.

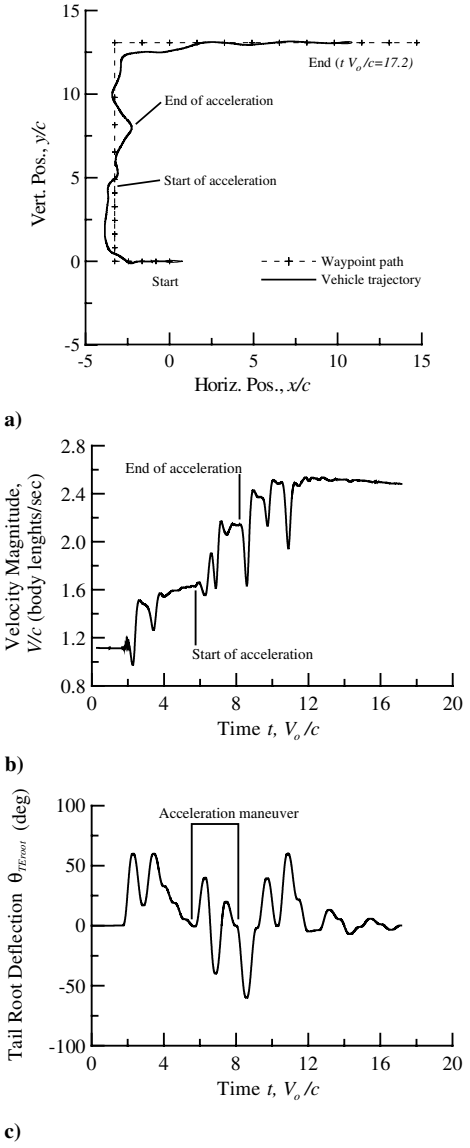

Fig. 18 Vehicle response during a combined navigation-acceleration test case: a) vehicle trajectory, b) tail root deflection history, and c) vehicle velocity profile.

3) The results of several case studies showed that the present method can handle various trajectories from sharp cornering to maintaining straight trajectories.

4) The slower trajectory sampling resulted in unwanted vehicle oscillations about the path. Faster path sampling eliminated these oscillations.

5) The test cases also showed that the present method is useful in a range of initial vehicle velocities.

6) During the acceleration tests, it was noted that a fast start could be used to change the speed during navigation without affecting the navigation.

7) It can be seen that the fast start can reach a steady velocity in significant less time and with less effort than a swimming start.

References

[1] Bandyopadhyay, P. R., "Maneuvering Hydrodynamics of Fish and Small Underwater Vehicles," *American Zoologist*, Vol. 40, No. 6, 2000, pp. 935–945.

[2] Galls, S. F., and Rediniotis, O. K., "Computational Simulation of the Autonomous Navigation of a Biomimetic Underwater Vehicle," *AIAA Journal*, Vol. 41, No. 4, 2003, pp. 605–611.

[3] Galls, S. F., "Development of a Computational Model for an Underwater Autonomous Vehicle," Ph.D. Dissertation, Texas A&M Univ., Dept. of Aerospace Engineering, Aug. 2001.

[4] Lighthill, M. J., "Swimming of Slender Fish," *Journal of Fluid Mechanics*, Vol. 9, May 1960, pp. 305–317.

[5] Jones, K. D., and Platzer, M. F., "Experimental and Numerical Investigation of Flapping-Wing Propulsion," AIAA Paper 99-0995, Jan. 1999.

[6] DeLaurier, J. D., and Harris, J. M., "Experimental Study of Oscillating-Wing Propulsion," *Journal of Aircraft*, Vol. 19, No. 5, 1982, pp. 368–373.

[7] Kelly, H. R., "Fish Propulsion Hydrodynamics," *Developments in Mechanics*, Vol. 1, Plenum, New York, 1961, pp. 442–450.

[8] Weihs, D., "Hydromechanical Analysis of Fish Turning Manoeuvres," *Proceedings of the Royal Society of London (B)*, Vol. 182, No. 1066, 1972, pp. 59–72.

[9] Beddow, T. A., van Leeuwen, J. L., and Johnston, I. A., "Swimming Kinematics of Fast Starts are Altered by Temperature Acclimation in the Marine Fish Myoxocephalus Scorpius," *Journal of Experimental Biology*, Vol. 198, Jan. 1995, pp. 203–208.

[10] McClelland, J., and Rumelhart, D., *Parallel Distributed Processing*, Vols. 1–2, MIT Press, Cambridge, MA, 1986.

[11] Schreck, S. J., Faller, W. E., and Luttges, M. W., "Neural Network Prediction of Three-Dimensional Unsteady Separated Flow Fields," AIAA Paper No. 93-3426-CP, August 1993.

[12] Schreck, S. J., and Faller, W. E., "Encoding of Three-Dimensional Unsteady Separated Flow Field Dynamics in Neural Network Architectures," AIAA Paper 95-0103, Jan. 1995.

[13] Rohloff, T. J., "Development and Evaluation of Neural Network Flush Airdata Sensing Systems," Ph.D. Dissertation, Univ. of California Los Angeles, Dept. of Mechanical Engineering, May 1998.

[14] Fan, X., Herbert, T., and Haritonidis, J. H., "Transition Control with Neural Networks," AIAA Paper 95-0674, Jan. 1995.

[15] Kinser, R. E., and Rediniotis, O. K., "Development of a Nearly Omni-Directional, Three-Component Velocity Measurement Pressure Probe," *AIAA Journal*, Vol. 36, No. 10, Oct. 1998, pp. 1854–1860.

[16] Vijayagopal, R., and Rediniotis, O. K., "Miniature Multi-Hole Pressure Probes and Their Neural-Network-Based Calibration," *AIAA Journal*, Vol. 37, No. 6, June 1999, pp. 666–674.

[17] Rediniotis, O., Wilson, L., Lagoudas, D., and Khan, M., "Development of a Shape-Memory-Alloy Actuated Biomimetic Hydrofoil," *Journal of Intelligent Material Systems and Structures*, Vol. 13, No. 1, Jan. 2002, pp. 35–49.

[18] Basu, B. C., and Hancock, G. J., "Unsteady Motion of a Two-Dimensional Aerofoil in Incompressible Inviscid Flow," *Journal of Fluid Mechanics*, Vol. 87, July 1978, pp. 159–178.

[19] Burden, L. R., and Faires, J. D., *Numerical Analysis*, 6th ed., Brooks, New York, 1997, pp. 294–305.

[20] Bisplinghoff, R. L., Ashley, H., and Halfman, R. L., *Aeroelasticity*, Dover, New York, 1996, pp. 251–281.

[21] Featherstone, R., "Calculation of Robot Dynamics Using Articulated Body Inertias," *International Journal of Robotics Research*, Vol. 2, No. 1, 1983, pp. 13–30.

[22] Ginsberg, J. H., *Advanced Engineering Dynamics* , Harper & Row, New York, 1988, pp. 305–307.

[23] Blom, F. J., and Leyland, P. , "Analysis of Fluid-Structure Interaction by Means of Dynamic Unstructured Meshes," *Journal of Fluids Engineering*, Vol. 120, No. 4, 1998, pp. 792–795.

K. Fujii
Associate Editor